

NONLINEAR COMBUSTION STABILITY PREDICTION WITH SPP/SSP*

J.C. French[†]
Software and Engineering Associates, Inc.
Carson City, NV

G.A. Flandro[‡]
The University of Tennessee Space Institute
Tullahoma, TN

ABSTRACT

Solid rocket motors experience combustion stability problems when the interior acoustic modes become coupled with combustion processes. Current linear analysis codes can predict if a SRM will be unstable, but do not predict severity of the instability. Nonlinear analysis incorporates higher order nonlinear damping terms, which become significant once a motor has become unstable and the oscillations attain higher amplitudes. Software and Engineering Associates, Inc., has integrated a nonlinear combustion stability module into the Solid Propellant Performance code (SPP) and the 1-D Standard Stability Prediction program (SSP). We have also taken steps to improve the underlying linear analysis, as several major changes in the analytical approach are required. The most important of these are allowing rotational flow effects and nonisentropic processes; the classical approach assumes irrotational, isentropic gas motion. In this way, one can accommodate the wave steepening process and the accompanying dissipative losses and unsteady conduction heat transfer effects in a direct way. Inclusion of the dissipative effect plays a major role in calculating the mean pressure shift that accompanies high-amplitude unsteady gas oscillations. The DC shift calculation must be accomplished in parallel with the nonlinear stability computations because the two mechanisms are strongly interconnected. That is, the shifting mean pressure has a profound effect on the magnitude of the limit amplitude and on triggering processes. Similarly, the mechanisms such as wave steepening into shocklike form plays a major role in controlling the magnitude of the DC shift.

INTRODUCTION

Solid rocket motor combustion instability occurs when combustion processes and the mean flow inside the rocket motor become coupled with the acoustic modes of the combustion chamber. The JANNAF Standard Stability Prediction program (SSP) was developed to predict SRM stability. It can only predict if a motor might be unstable, as it is based on a linear stability analysis of the motor. Once a motor goes unstable, it can either explode or enter a limited amplitude pressure cycle, during which the pressure oscillates about a DC pressure shift. Prediction of the maximum pressure amplitude requires a nonlinear analysis of the interaction between the combustion processes, the mean flow and the acoustics of the combustion chamber.

Under a Navy SBIR,^{*} SEA has sought to couple the Solid Performance Program (SPP) and the Standard Stability Prediction program (SSP) with a nonlinear analysis module. It is our intent to develop a nonlinear stability module that will predict the following: the amplitude of the pressure oscillation, the DC shift in the oscillation, and the potential for events to trigger otherwise stable motors into an unstable regime. At the same time, we have also sought to improve the linear stability analysis, as the nonlinear analysis is only as accurate as the underlying linear analysis. We briefly review the linear improvements herein, applied to the Advanced Solid Rocket Motor (ASRM) and Dr. Blomshield's star-aft test motor.³

At present, SEA has developed a nonlinear analysis module following the approach of Dr. Fred Culick.^{1,2} SSP passes the linear stability analysis, including the 1D mode shapes, to the nonlinear

© Software and Engineering Associates, Inc. Published by the Chemical Propulsion Information Agency with permission.

* This effort was performed under Navy SBIR contract no. N68936-02-C-0868.

[†] Senior Engineer

[‡] UTSI Professor, Boling Chair of Excellence in Space Propulsion

Distribution Statement - Approved for public release, distribution is unlimited

module. The nonlinear module integrates the nonlinear system of ODEs in time to determine the maximum oscillatory pressure amplitude. We plan to add a continuation code option, which will determine the global stability of the motor as a function of a given stability integral parameter. It is hoped that this option will allow us to predict triggering. We have also included a nonlinear analysis of the ASRM and the star-aft test motor.

SEA is also carrying out improvements to the linear and nonlinear theory. Dr. Gary Flandro of UTSI has reformulated the underlying analytical approach to include the effects of rotational flow and nonisentropic processes that are neglected in the classical SSP modeling. These changes improve the linear results by incorporating stability integral components that are lost as a result of oversimplification of the basic formulation. For example, inclusion of rotational (vortical) flow effects clarifies the origin of the important Culick flow-turning damping stability integral, which was found previously only in its one-dimensional form. The new analysis reveals that the flow-turning loss is the result of rotational flow processes at burning surfaces that appear when correct boundary conditions (the no-slip condition) are applied. In this way one recovers the three-dimensional form of the flow-turning damping integral, which was previously represented in general calculations by patching on the one-dimensional result. Additional corrective stability terms are also found which demonstrably improve the agreement between the SSP predictions and experimental data. In order to reduce computational complexity, work is underway to represent all stability integrals in surface integral form. Then the need for complex analysis of the full rotational flow field in the chamber can be relaxed. All rotational flow effects are readily treated in terms of the more readily calculated acoustic pressure and pressure gradient effects at the chamber surfaces.

A new nonlinear analytical formulation is under development. A major change in philosophy is relaxation of the often used isentropic flow assumption, which makes it necessary to employ the complete energy equation including heat transfer and dissipation function effects. When this is done, it becomes possible to trace in detail the origin and behavior of important nonlinear effects leading to limit cycle oscillations, triggering and the important DC shift phenomenon. The final result will significantly improve the predictive and diagnostic capabilities of the SSP. It will then be possible to predict not only the system stability characteristics, but also the far more important limit cycle and triggering amplitudes. Of great interest to motor designers will be the capability to predict the magnitude of the DC shift, which remains an unsolved problem and a major threat to motor structural integrity.

RESULTS AND DISCUSSION

SEA maintains design codes, which by their nature must run quickly to be of practical use in the design cycle. This leads us to prefer an analytic solution to the stability problem, rather than a Navier-Stokes time domain approach. We have investigated several analytic approaches to combustion stability analysis,^{2,8,9} and they all require an accurate analysis of the motor's linear stability.

LINEAR STABILITY ANALYSIS IMPROVEMENTS

We have evaluated our linear analysis improvements using the ASRM¹ (Figure 1) and Dr. Fred Blomshield's star-aft test motor³ (Figure 9). Both of these motors are unclassified. We have made improvements in the code that translates data from SPP to SSP, and we refer to code that connects different modules as "linkages". We will refer to the 1987 SPP / SSP linkage as the "original" linkage, and our current efforts as the "improved grain design" linkage.

When SSP was first incorporated into SPP, it was modified as little as possible, and the data from SPP was interpolated onto SSP's fixed axial mesh locations. SSP was limited to only 40 axial stations in order to reduce run times and memory requirements. Our most significant recent improvement to the SSP code has been to increase the number of axial stations so that SSP can use the same mesh as SPP, and the associated grain design and ballistics data at each station. This yielded a two-fold benefit. Not only do we no longer have to interpolate the SPP data onto the SSP mesh, but we can also accurately model the burning of radial slots in SSP using the SPP XSLOT option. We have modified the linkage algorithm so that SSP can recognize when a slot occurs. At slot locations, SSP can now insert an

additional axial station at the discontinuity location to capture the effect of the slot on the acoustic mode shape.

Improvements to the axial fidelity can be seen in Figure 2 and Figure 10, in which the axial cross sections follow the contours of the grain design more tightly. The improved axial fidelity also helps SSP track radial slots, which can be seen in the original and improved perimeters of Figure 3 and Figure 11. These figures show that in regions of sudden variation, such as near slots, the original SSP linkage does not resolve the slot regions well. These improvements also significantly changed the computed frequency and overall stability of the motor Figure 7 and Figure 15. The original SSP did a better job analyzing Blomshield's test motor acoustics and steady velocity (Figure 12-Figure 14) than it did with the ASRM (Figure 4-Figure 6). This was primarily due to the difficulty the original linkage has in evaluating the ASRM's radial slots.

We should also note that we fixed an error in the SPP burning perimeter computation used in the "original" linkage formulation, so that the results presented herein for the "original" linkage are better than those presented in Ref. 1. In particular, the mean velocity parameter, which in the original linkage SSP re-computes based on the burning perimeter rather than obtaining it from the SPP ballistics, now matches the improved linkage results more closely (Figure 6). This has resulted in a much better correlation between the original and improved linkage overall stability analyses than that of Ref. 1. The mean velocity is a particularly important stability parameter, as the nozzle damping term is linearly proportional to the mean velocity as shown in Equation (1). In Figure 8 we compare the original linkage results and the improved linkage results with the original linkage without the perimeter fix. The ASRM was particularly effected due to the radial slots and the large number of "deep" head end axial slots.

$$\alpha_m = \frac{1}{2E_n^2} R_N u_N \hat{p}_m^2 S_N \quad (1)$$

(R_N is the nozzle response function, u_N is the mean velocity at the nozzle entrance, S_N is the cross-sectional area at the nozzle entrance.)

With Dr. Flandro's help, SEA has incorporated his rotational velocity correction term into SSP.^{4,5} The inclusion of this term reduces the computed stability, but to varying amounts depending on the grain design configuration. The volume integral form of this parameter is:

$$\alpha_5 = \frac{1}{2E_m^2} \iiint_V (\tilde{u}_m \cdot \nabla \hat{p}_m) dV \quad (2)$$

(E_m is a normalization parameter, V is the volume, m is the acoustic mode #, \tilde{u} is the perturbed rotational velocity, and \hat{p} is the acoustic mode shape) This may be simplified to a surface integral using the following identity:

$$\nabla \cdot (\tilde{u} \hat{p}) = \tilde{u} \cdot \nabla \hat{p} + \hat{p} \nabla \cdot \tilde{u} = \tilde{u} \cdot \nabla \hat{p} \quad (3)$$

$$\alpha_5 = \frac{1}{2E_m^2} \iiint_V (\tilde{u}_m \cdot \nabla \hat{p}_m) dV = \frac{1}{2E_m^2} \iiint_V \nabla \cdot (\tilde{u}_m \hat{p}_m) dV = \iint_S \bar{n} \cdot \tilde{u}_m \hat{p}_m dV \quad (4)$$

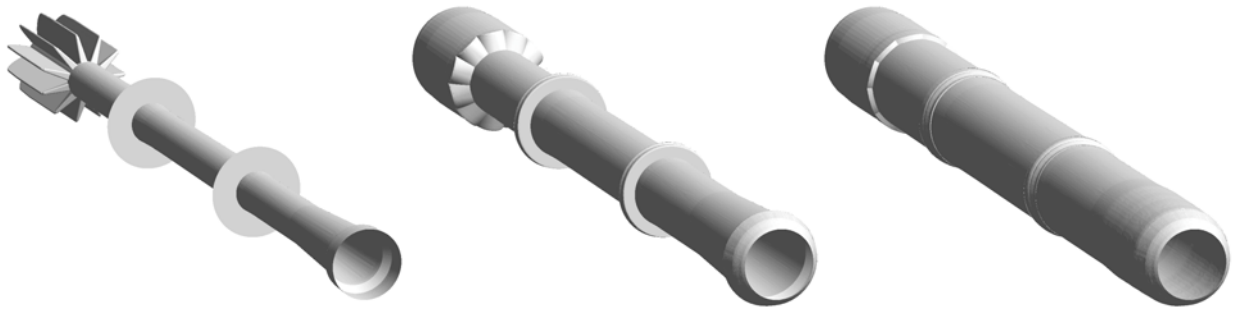
(\bar{n} is the surface normal). Flandro has determined that the normal component of the rotational velocity (\tilde{u}_r) is proportional to the product of the mass injection velocity and the acoustic mode shape:⁵

$$\bar{n} \cdot \tilde{u} = \tilde{u}_r = u_b \hat{p} \quad (5)$$

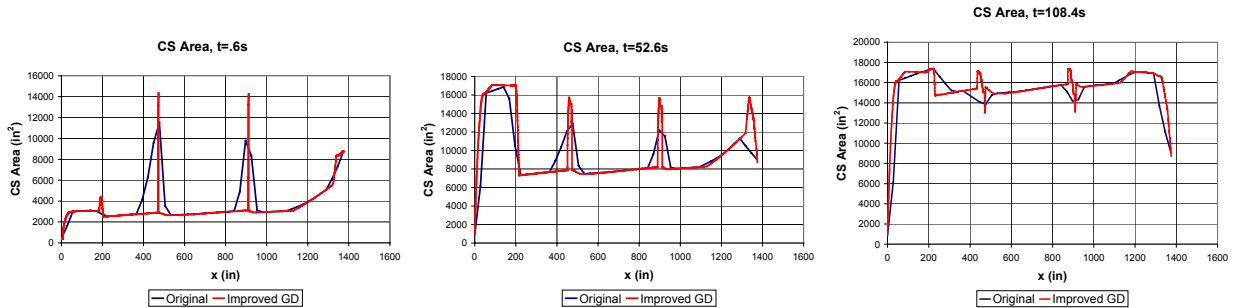
This simplifies (4):

$$\alpha_5 = \frac{1}{2E_m^2} \iint_S u_b \hat{p}_m^2 dV \quad (6)$$

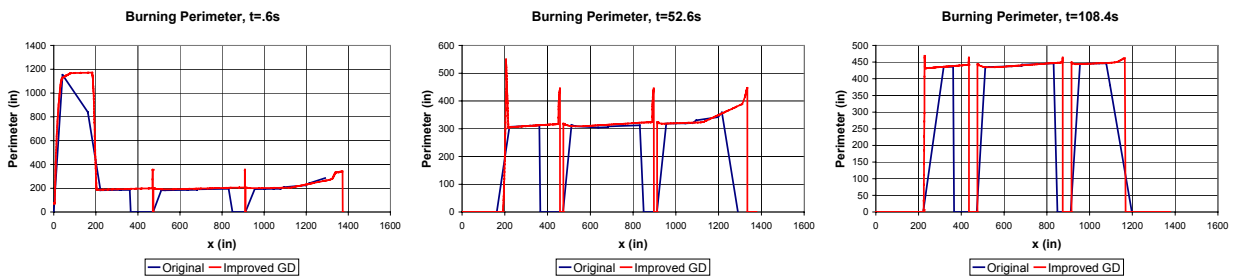
This stability integral is similar to the pressure coupling term, but without the response function parameter. It is easily utilized with both the original and improved linkages, and is shown in Figure 8b and Figure 16b. It actually shifted the stability margin positive briefly for both the ASRM and the test motor (Figure 7 and Figure 15). We plan to incorporate other rotational flow correction terms as they become available. Dr. Flandro and Dr. Majdalani have additional rotational corrections,⁵ but they are difficult to incorporate into the code because the stability integrals are volume integrals containing rotational flow parameters, parameters which we have not computed away from the surface. Once the volume integrals are reduced to surface integrals, the rotational velocity parameter may be approximated as in Equation (5). An alternative approach we have considered is to compute the perturbed rotational flow field (the complement of the acoustic irrotational field). We are currently evaluating this approach, but this becomes a formidable task when one tries to enforce the zero divergence restriction on the rotational velocity field.



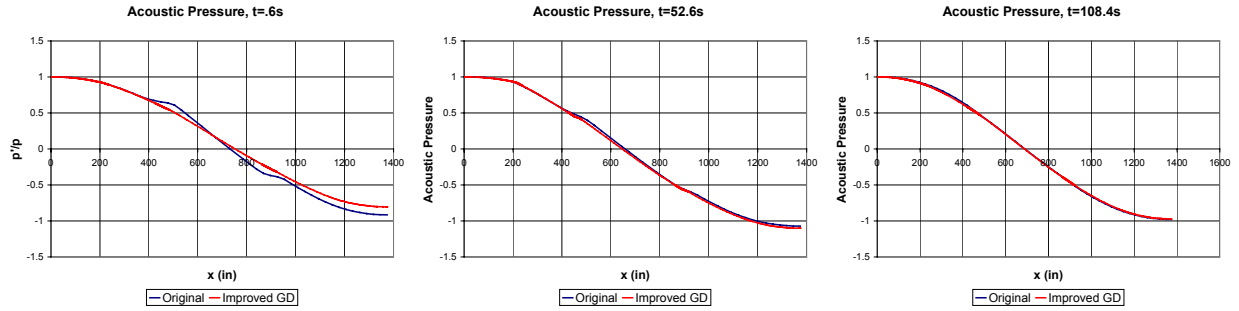
(a) Time = .6 seconds (b) Time = 52.6 seconds (c) Time = 108.4 seconds
Figure 1. ASRM burn back at different time steps



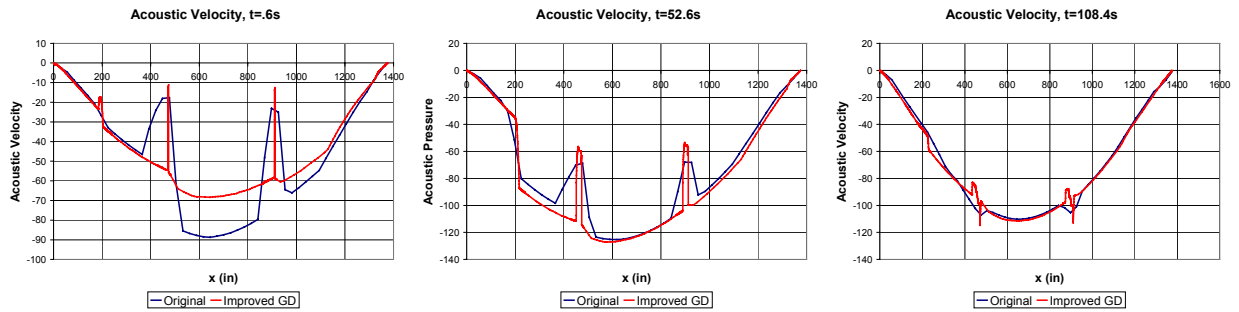
(a) Time = .6 seconds (b) Time = 52.6 seconds (c) Time = 108.4 seconds
Figure 2. ASRM: Comparison of original and improved grain design linkage effects on cross-sectional area



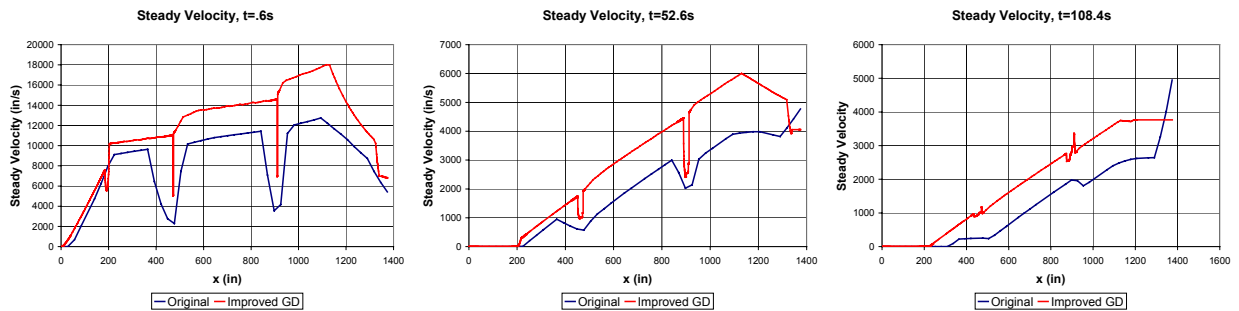
(a) Time = .6 seconds (b) Time = 52.6 seconds (c) Time = 108.4 seconds
Figure 3. ASRM: Comparison of original and improved grain design linkage effects on burning perimeter



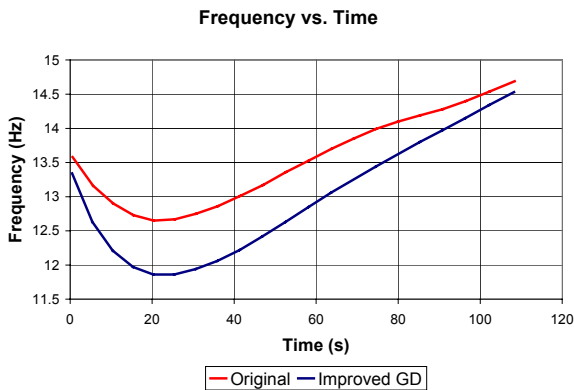
(a) Time = .6 seconds (b) Time = 52.6 seconds (c) Time = 108.4 seconds
 Figure 4. ASRM: Comparison of original and improved grain design linkage effects on first acoustic pressure mode shape



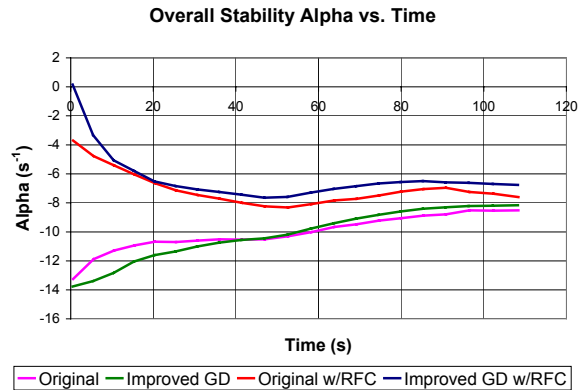
(a) Time = .6 seconds (b) Time = 52.6 seconds (c) Time = 108.4 seconds
 Figure 5. ASRM: Comparison of original and improved grain design linkage effects on first acoustic velocity mode shape



(a) Time = .6 seconds (b) Time = 52.6 seconds (c) Time = 108.4 seconds
 Figure 6. ASRM: Comparison of original and improved grain design linkage effects on steady velocity

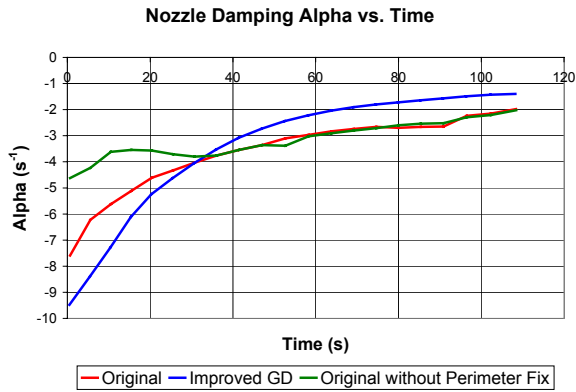


(a) Frequency variation over time

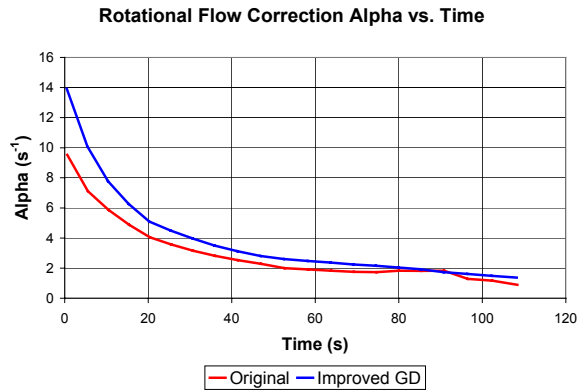


(b) Overall stability variation over time

Figure 7. ASRM: Comparison of original and improved grain design linkage effects on frequency and stability

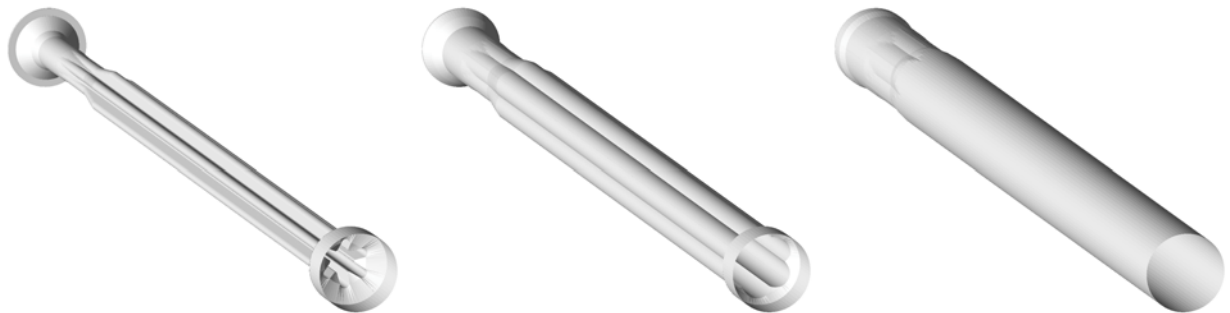


(a) Nozzle Damping



(b) Rotational Flow Correction

Figure 8. ASRM: Selected individual stability integrals

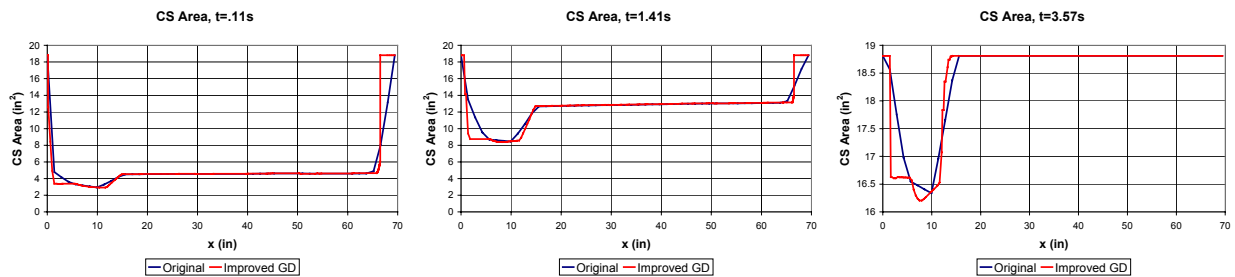


(a) Time = .11 seconds

(b) Time = 1.41 seconds

(c) Time = 3.57 seconds

Figure 9. Star-aft test motor burn back at different time steps

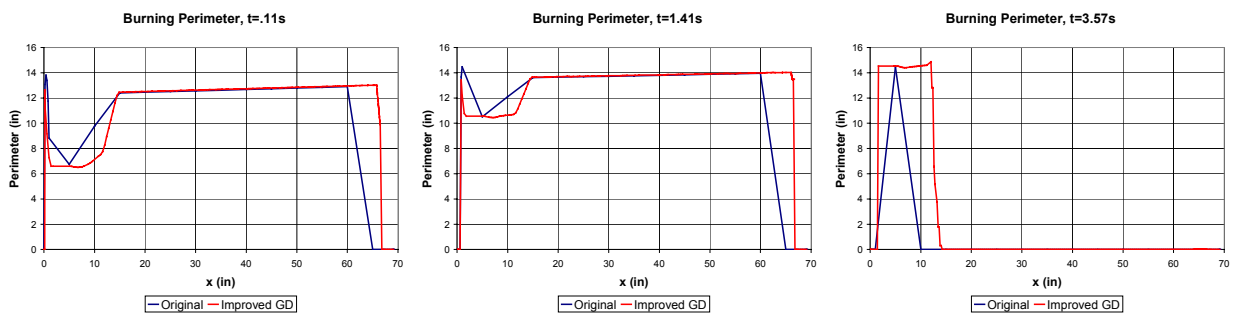


(a) Time = .11 seconds

(b) Time = 1.41 seconds

(c) Time = 3.57 seconds

Figure 10. Star-aft test motor: Comparison of original and improved grain design linkage effects on cross-sectional area

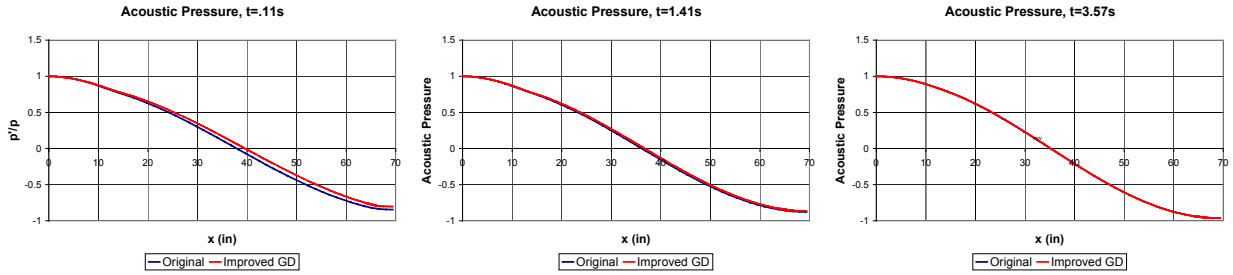


(a) Time = .11 seconds

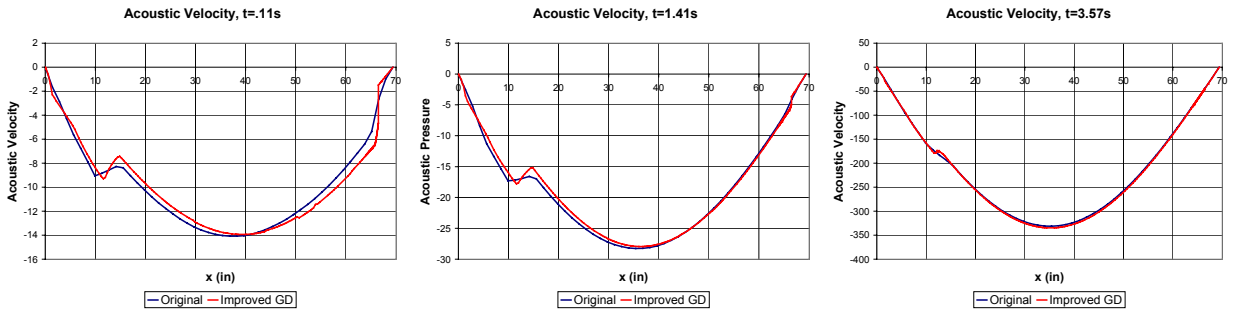
(b) Time = 1.41 seconds

(c) Time = 3.57 seconds

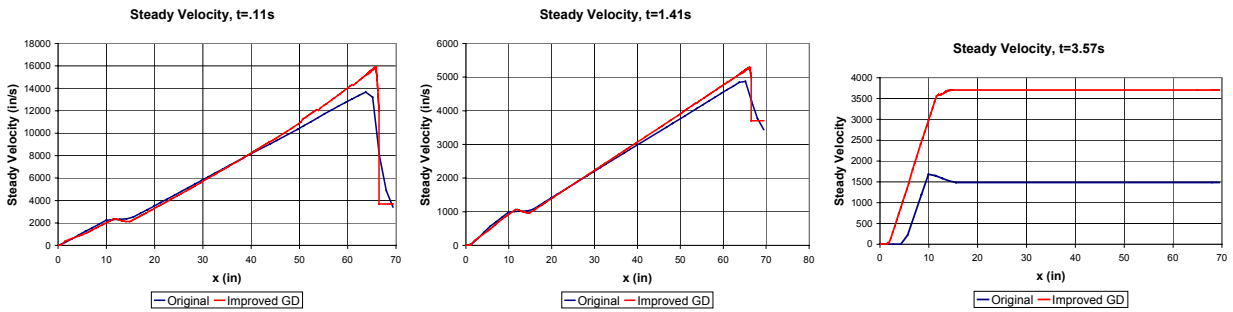
Figure 11. Star-aft test motor: Comparison of original and improved grain design linkage effects on burning perimeter



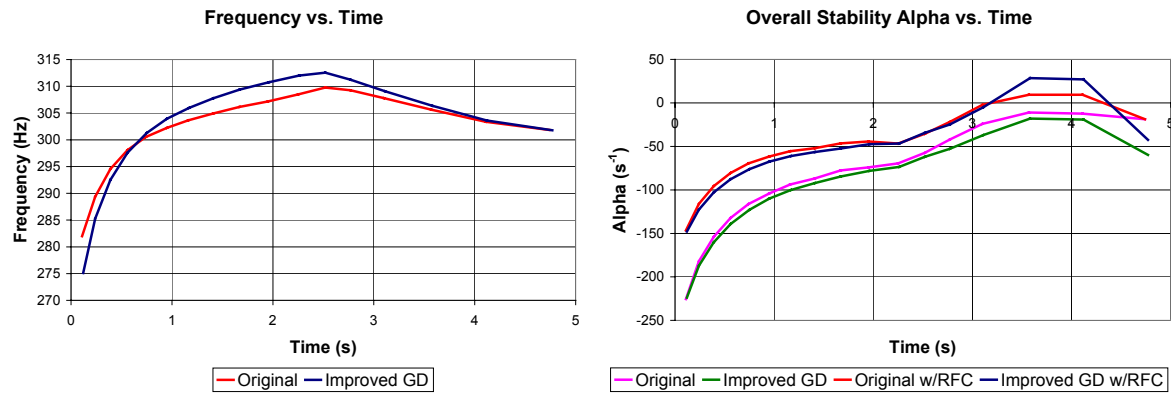
(a) Time = .11 seconds (b) Time = 1.41 seconds (c) Time = 3.57 seconds
 Figure 12. Star-aft test motor: Comparison of original and improved grain design linkage effects on first acoustic pressure mode shape



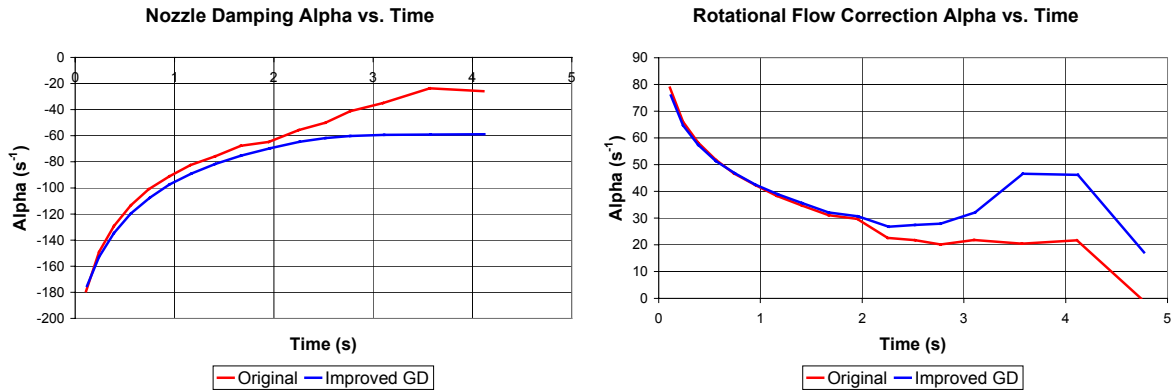
(a) Time = .11 seconds (b) Time = 1.41 seconds (c) Time = 3.57 seconds
 Figure 13. Star-aft test motor: Comparison of original and improved grain design linkage effects on first acoustic velocity mode shape



(a) Time = .11 seconds (b) Time = 1.41 seconds (c) Time = 3.57 seconds
 Figure 14. Star-aft test motor: Comparison of original and improved grain design linkage effects on steady velocity



(a) Frequency variation over time (b) Overall stability variation over time
 Figure 15. Star-aft test motor: Comparison of original and improved grain design linkage effects on frequency and stability



(a) Nozzle Damping (b) Rotational Flow Correction
 Figure 16. Star-aft test motor: Selected individual stability integrals

NONLINEAR STABILITY ANALYSIS

SEA has incorporated Dr. Culick's approach to nonlinear stability into a module called by SSP.¹ It is an extension of the linear analysis which retains the higher order nonlinear terms.² Culick's approach uses separation of variables to derive a system of ordinary differential equations (ODEs) composed of time-dependent amplitude functions (one per mode). The ODEs are linked in the nonlinear gas dynamics and combustion response terms. The system can be integrated forward in time to predict the limiting amplitudes, or a continuation code can be used to predict the limiting amplitude as a function of the unstable mode's overall exponential growth rate. The latter approach allows the analyst to evaluate the extent to which stability improvement is needed.

We have again applied the analysis to the problems of the ASRM and the star-aft test motor. In both cases, we have used 20 acoustic modes, which following Culick's approach is transformed into a linear system of 40 ODEs. This system of equations is solved by integrating in time until a steady state "limiting amplitude" is reached. In our test cases, we chose points during the burn at which SSP predicted each motor would be unstable. SSP passes the linear stability information, including the stability alphas and the pressure mode shapes to the nonlinear module.

One caveat of Culick's analysis is that it requires the imaginary portion of the response function in order to incorporate the linear phase shift (the imaginary complement of the stability alpha). As this response function is not easily obtained, we did a analysis to determine if it is needed to predict limiting amplitudes. We first fixed the linear phase shifts all to zero, and then set it to random values. We used Blomshield's test motor as our test case, and found that the limiting amplitude was reached regardless of the linear stability values. Therefore we are fixing the linear phase shifts to zero, until we find a compelling reason not to do so.

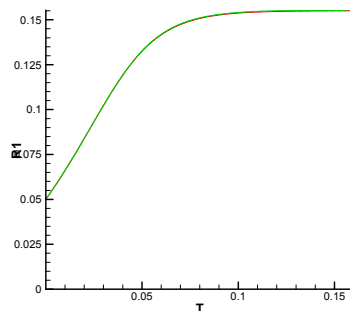


Figure 17. Star-aft motor: 1st mode amplitude with and without linear phase shift

We are currently implementing a continuation code in order to predict the nonlinear stability of a motor as a function of the first overall stability integral. This will allow one to see how the limiting amplitude varies as a function of the stability parameter, and it is hoped that this will also lead to the prediction of triggering. The continuation code can be run in two modes: static and periodic. The static mode presumes that a stationary solution can be found to the system of ODEs, while the periodic mode presumes the solution will vary with time in a periodic fashion. As the periodic mode is more computationally intensive, we have sought to find a stationary solution to the oscillation equations. If one transforms the ODEs into a system of time varying amplitudes and phase shifts, once a steady state is reached, the amplitude should become constant. In computational experiments with a cylindrical grain, the amplitude did become constant, but the phase varied in a predictable way: each mode's phase variation was the product of the mode number and the first mode's phase variation.⁷ This predictable relationship between the phase variations allowed Dr. Culick to transform the phase variation to a new parameter that did have zero time variation. We were able to reproduce their results. However, when we went to apply the transformation to non-cylindrical grain designs, we found that the transform did not apply in these situations, and that there did not appear to be any predictable transform that could be used to eliminate their phase variation in time. We have conjectured that this might be due to an error in the time averaging over the first period for non-cylindrical motors.⁶

We have re-derived the underlying ordinary differential equations to eliminate the time averaging, and modified the code to solve for this new system of equations. The standard derivation chooses the relationship between the amplitude and the phase variation⁷:

$$\begin{aligned} \dot{r}_n \sin(\omega_n t + \phi_n) + r_n \dot{\phi}_n \cos(\omega_n t + \phi_n) &= 0 \\ \dot{\phi}_n &= -\frac{\dot{r}_n}{r_n} \tan(\omega_n t + \phi_n) \end{aligned} \quad (7)$$

This assumption can then be used to simplify the system of ODEs without resorting to time averaging:

$$\begin{aligned} \dot{r}_n \cos(\omega_n t + \phi_n) - r_n \dot{\phi}_n \sin(\omega_n t + \phi_n) &= F_n / \omega_n \\ \dot{r}_n \cos(\omega_n t + \phi_n) - r_n \left(-\frac{\dot{r}_n}{r_n} \tan(\omega_n t + \phi_n) \right) \sin(\omega_n t + \phi_n) &= F_n / \omega_n \\ \dot{r}_n \left[\cos(\omega_n t + \phi_n) + \frac{\sin^2(\omega_n t + \phi_n)}{\cos(\omega_n t + \phi_n)} \right] &= F_n / \omega_n \\ \dot{r}_n &= F_n / \omega_n \cos(\omega_n t + \phi_n) \\ \dot{\phi}_n &= -\frac{F_n \sin(\omega_n t + \phi_n)}{\omega_n r_n} \end{aligned} \quad (8)$$

This lets us solve directly for the time variation in the amplitude and the phase. However, solutions from this system of ODEs are still oscillatory (even the amplitude has small oscillations), and the continuation code needs to have a non-oscillatory solution. If we cannot eliminate the oscillations, we will need to use the continuation code in its oscillatory (or periodic) mode, which takes longer. The above system of ODEs is less computationally intensive in contrast to the time averaging approach for non-cylindrical grain designs.

We have noted that while the acoustic modes appear to act independently, if they are superimposed they often coalesce into steeply fronted traveling waveforms over time. This is what Flandro has previously predicted would happen as the result of an entropy loss across the steeply fronted wave.^{8,9}

The following is a brief description of the new analysis with emphasis on predicting the mean pressure (DC pressure) shift phenomenon. When the irrotational and isentropic flow assumptions are removed, the governing equations (continuity, momentum, energy, state) in dimensionless form become:

$$\left\{ \begin{array}{l} \frac{\partial \rho}{\partial t} + \nabla \cdot \rho \mathbf{u} = 0 \end{array} \right. \quad (9)$$

$$\left\{ \begin{array}{l} \rho \left[\frac{\partial \mathbf{u}}{\partial t} + \frac{1}{2} \nabla \mathbf{u} \cdot \mathbf{u} - \mathbf{u} \times \boldsymbol{\omega} \right] = -\frac{1}{\gamma} \nabla p - \delta^2 \nabla \times \nabla \times \mathbf{u} + \delta_d^2 \nabla (\nabla \cdot \mathbf{u}) + \mathbf{F} \end{array} \right. \quad (10)$$

$$\left\{ \begin{array}{l} \rho \left[\frac{\partial T}{\partial t} + \mathbf{u} \cdot \nabla T \right] = \frac{(\gamma-1)}{\gamma} \left[\frac{\partial p}{\partial t} + \mathbf{u} \cdot \nabla p \right] + \left[\frac{\delta^2}{Pr} \nabla^2 T + \delta^2 (\gamma-1) \boldsymbol{\omega} \cdot \boldsymbol{\omega} + \delta_d^2 (\gamma-1) (\nabla \cdot \mathbf{u})^2 \right] + (\gamma-1) \mathbf{F} \cdot \mathbf{u} \end{array} \right. \quad (11)$$

$$\left\{ \begin{array}{l} p = \rho T \end{array} \right. \quad (12)$$

where Pr is the Prandtl number and

$$\delta^2 = \frac{v}{a_0 R} \quad \text{and} \quad \delta_d^2 = \delta^2 \left(\frac{\eta}{\mu} + \frac{4}{3} \right)$$

are Reynolds numbers based on the speed of sound, chamber size, and coefficients of viscosity and bulk viscosity. Notice that all convective and conduction heat transfer terms are retained as well as rotational flow effects in the momentum balance, Eq. (10) and in the Rayleigh dissipation function in the energy equation, Eq. (11). In setting up the problem for stability computations, it is useful to decompose the variables into quasi-steady and unsteady parts:

$$\left\{ \begin{array}{l} \rho = \bar{\rho} + \varepsilon \rho' \\ p = \bar{p} + \varepsilon p' \\ T = \bar{T} + \varepsilon T' \\ \mathbf{u} = M_b \mathbf{U} + \varepsilon \mathbf{u}' \\ \boldsymbol{\omega} = M_b \nabla \times \mathbf{U} + \varepsilon \nabla \times \mathbf{u}' = M_b \boldsymbol{\Omega} + \varepsilon \boldsymbol{\omega}' \end{array} \right. \quad (13)$$

where the overbar indicates variables that change slowly with time in a nonoscillatory way and primes denote the oscillatory variables. The mean temperature and speed of sound are assumed constant. A major goal is to predict the mean pressure changes and to relate them to the DC shift.

It is useful to eliminate the temperature and density variables by combining Eqs. (9), (11), and (12). Then the pressure becomes the governing thermodynamic variable in keeping with the traditional approach. The motion is then governed by

$$\left\{ \begin{array}{l} \frac{\partial p}{\partial t} + \mathbf{u} \cdot \nabla p + \gamma p \nabla \cdot \mathbf{u} = \gamma \left[\frac{\delta^2}{Pr} \nabla^2 T + \delta^2 (\gamma-1) \boldsymbol{\omega} \cdot \boldsymbol{\omega} + \delta_d^2 (\gamma-1) (\nabla \cdot \mathbf{u})^2 \right] + \gamma (\gamma-1) \mathbf{F} \cdot \mathbf{u} \end{array} \right. \quad (14)$$

$$\left\{ \begin{array}{l} \rho \frac{\partial \mathbf{u}}{\partial t} + \frac{1}{\gamma} \nabla p = -\rho \left[\frac{1}{2} \nabla \mathbf{u} \cdot \mathbf{u} - \mathbf{u} \times \boldsymbol{\omega} \right] - \delta^2 \nabla \times \nabla \times \mathbf{u} + \delta_d^2 \nabla (\nabla \cdot \mathbf{u}) + \mathbf{F} \end{array} \right. \quad (15)$$

Equation (14) now takes the place of the usual form of the continuity equation with pressure replaced by density using the isentropic assumption. Starting with these equations, and improved stability analysis can be constructed by following methods introduced by Culick. For example, after inserting Eqs. (13) and neglecting time varying steady variables, (14) and (15) can be combined to form the perturbed acoustic wave equation in the traditional fashion. This will not be done here. Instead, we take this opportunity to illustrate the method for computing the DC pressure shift.

Insert Eqs. (13) into Eq. (14) and separate the quasi-steady and unsteady parts by taking the time average. The quasi-steady component becomes:

$$\frac{d\bar{P}}{dt} = \left\langle \begin{aligned} & -\nabla \cdot (M_b \bar{P} \mathbf{U} + \varepsilon^2 p' \mathbf{u}') - (\gamma - 1) (M_b \bar{P} \nabla \cdot \mathbf{U} + \varepsilon^2 p' \nabla \cdot \mathbf{u}') + \\ & + \delta_d^2 \gamma (\gamma - 1) [\varepsilon^2 (\nabla \cdot \mathbf{u}')^2] + \delta^2 \gamma (\gamma - 1) [\varepsilon^2 \boldsymbol{\omega}' \cdot \boldsymbol{\omega}'] \end{aligned} \right\rangle \quad (16)$$

where the triangular brackets denote the time average. This equation then reduces to an equation for the rate of change of the mean pressure:

$$\frac{d\bar{P}}{dt} = \left\{ \begin{aligned} & -M_b [\nabla \cdot (\bar{P} \mathbf{U}) + (\gamma - 1) \bar{P} \nabla \cdot \mathbf{U}] + \varepsilon^2 \left[-\nabla \cdot \langle p' \mathbf{u}' \rangle - (\gamma - 1) p' \nabla \cdot \mathbf{u}' + \right. \\ & \left. + \delta_d^2 \gamma (\gamma - 1) \langle (\nabla \cdot \mathbf{u}')^2 \rangle + \delta^2 \gamma (\gamma - 1) \langle \boldsymbol{\omega}' \cdot \boldsymbol{\omega}' \rangle \right] \end{aligned} \right\} \quad (17)$$

where all nonlinear terms have been retained. In order to achieve a correct mass balance, it is necessary to account for all mass flux entering and leaving the chamber control volume. This is most easily accomplished by integrating Eq. (17) over the chamber volume and using Gauss's theorem with the result

$$\frac{d\bar{P}}{dt} = \frac{1}{\bar{V}} \left\{ \begin{aligned} & -\gamma M_b \bar{P} \iint_S \mathbf{n} \cdot \mathbf{U} dS - \varepsilon^2 \iint_S \mathbf{n} \cdot \langle p' \mathbf{u}' \rangle dS \\ & -\varepsilon^2 (\gamma - 1) \iiint_V \langle p' \nabla \cdot \mathbf{u}' \rangle dV + \varepsilon^2 \delta_d^2 \gamma (\gamma - 1) \iiint_V \langle (\nabla \cdot \mathbf{u}')^2 \rangle dV \\ & + \varepsilon^2 \delta^2 \gamma (\gamma - 1) \iiint_V \langle \boldsymbol{\omega}' \cdot \boldsymbol{\omega}' \rangle dV \end{aligned} \right\} \quad (18)$$

The first term on the left represents the usual steady mass flux into the chamber from the burning surface and the outflow of mass through the nozzle. \bar{V} is the instantaneous chamber volume. In integrating Eq. (18) it is necessary to track the burning rate and resulting changes in burning surface area and combustion chamber volume as functions of time. Notice that in addition to the classical mass balance terms there appear four nonlinear terms. These are the principal source of the DC pressure rise and come into play as the amplitude of the wave motions (reflected in the amplitude parameter, ε) grows in time. The second term on the right of Eq. (18) is readily seen to contribute a positive net mass flux increase proportional to the propellant response function. Hence propellants that are more prone to support oscillatory behavior are also expected to exhibit a more pronounced DC shift. The two terms on the second line in Eq. (18) represent the effect of wave steepening on the DC pressure rise. Both yield positive contributions because, for example,

$$\langle p' \nabla \cdot \mathbf{u}' \rangle \approx - \left(\frac{\partial u'}{\partial x} \right)^2 \quad (19)$$

for an axial acoustic wave. In a real system it is necessary to account for a superposition of many acoustic modes. For example,

$$\left\{ \begin{array}{l} p' = \gamma p' = \varepsilon \sum_{n=1}^{\infty} A_n \cos(k_n x) \sin(k_n t) \\ u' = \varepsilon \frac{1}{\gamma} \sum_{n=1}^{\infty} B_n \sin(k_n x) \cos(k_n t) \end{array} \right. \quad k_n = \frac{n\pi R}{L}$$

As already pointed out, both experimental data and numerical results show that as the limit cycle is approached, the relative amplitudes of these modes become fixed; a steep fronted wave appears. Of greatest significance is that very large values for the pressure and velocity gradients appear at the instantaneous location of the traveling wave front. Figure 18 shows a typical snapshot of the velocity gradient as the wave passes the center of the chamber.

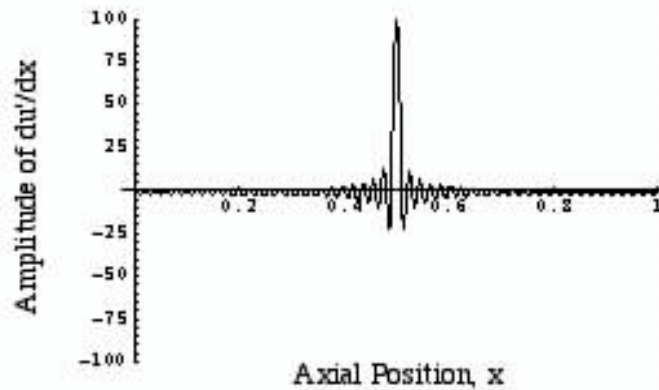


Figure 18. Amplitude of gradient of velocity as steep wavefront passes center of motor

It is clear that the square of this term leads to a major contribution to the development of the DC shift. The last term in Eq. (18) has not yet been fully evaluated, but it represents the production of unsteady vorticity at the surfaces leading again to a positive contribution to the growth of the pressure shift. The volume integral shown is readily converted to a surface integral. It may be significant because the amplitude of the unsteady vorticity is of the order of the inverse of the mean flow Mach number at the surface.

Finally, following an approach paralleling the one just illustrated, the system amplitude, $\varepsilon = \varepsilon(t)$ can be computed taking direct account again of the energy losses in the steep wave fronts, full vorticity interactions, and the heat transfer effects in the shock fronts. Preliminary results show that a practical and accurate method for predicting limit cycle amplitude and triggering is then achieved.

SUMMARY AND CONCLUSIONS

We have greatly improved the fidelity of the SPP / SSP linkage, allowing SSP to better model radial slots. Dr. Culick's nonlinear analysis approach is now integrated into SPP / SSP, and have used it to model behavior in the ASRM and Dr. Blomshield's star-aft test motor. It does not appear that the linear phase shift is a necessary parameter. If this holds true, the user will not need to obtain a propellant's imaginary response function data from an L* burner. From Dr. Flandro's work, we have a good start on a theoretical model for predicting the DC shift.

FUTURE WORK

We plan to implement additional rotational flow linear stability integrals to improve the accuracy of the linear analysis. We are adding a continuation code to help predict triggering, and will probably have to use the periodic solution approach. We also plan to incorporate Dr. Flandro's DC shift model into the SPP / SSP code.

ACKNOWLEDGEMENTS

We would first like to thank Fred Blomshield, of NAWC / China Lake, for his support in funding this effort. This paper would not have been possible without the groundbreaking work performed by Fred Culick, in the development of the system of ODEs. We also appreciate the help from Gary Flandro for breaking new ground in the quest to improve both linear and nonlinear combustion stability analyses.

REFERENCES

- ¹French, J.C., "Nonlinear Combustion Stability Prediction of SRMs Using SPP/SSP," 39th AIAA / ASME / SAE / ASEE Joint Propulsion Conference, Huntsville, AL, July 2003.
- ²Culick, F.E.C., and Yang, V., "Prediction of the Stability of Unsteady Motions in Solid Propellant Rocket Motors", Chapter 18 in *Nonsteady Burning and Combustion Stability of Solid Propellants*, Progress in Astronautics and Aeronautics, Vol. 143, 1992.
- ³Blomshield, F.S., "Pulsed Motor Firings", NAWCWD TP 8444, China Lake, August 2000.
- ⁴Flandro, G.A., *Effects of Vorticity on Rocket Combustion Stability*, AIAA Journal of Propulsion and Power, Vol. 11, No. 4, July-August 1995.
- ⁵Flandro, G.A., Majdalani, J., "Aeroacoustic Instability in Rockets", AIAA 2001-3868, 37th Joint Propulsion Conference, Salt Lake City, UT, OH, July 2001.
- ⁶French, J.C., "Nonlinear Combustion Stability Prediction Of Solid Rocket Motors: Contract Progress, Status, and Management Report", N68936-02-C-0868, Contractor's Progress and Status Report No. 9, October 2004
- ⁷Burnley, V.S., "Nonlinear Combustion Instabilities and Stochastic Sources", Thesis, California Institute of Technology, CA, 1996, p. 25.
- ⁸Flandro, G.A., "Approximate Analysis of Nonlinear Instability with Shock Waves", AIAA-82-1220, 18th Joint Propulsion Conference, Cleveland, OH, June 1982.
- ⁹Flandro, G.A., *Energy Balance Analysis of Nonlinear Combustion Instability*, , AIAA Journal of Propulsion and Power, Vol. 1, No. 3, May-June 1985.